Optical Fiber Technology 61 (2021) 102429

Contents lists available at ScienceDirect

Optical Fiber Technology

journal homepage: www.elsevier.com/locate/yofte

Design and simulation of a novel fungus-shaped center embossed diaphragm for fiber optic pressure sensors

Şekip Esat Hayber [a,*], Umut Aydemir [b,c]

[a] Department of Electrical-Electronics Engineering, Kırşehir Ahi Evran University, 40100 Kırşehir, Turkey
[b] Department of Electrical-Electronics Engineering, Uludağ University, 16120 Bursa, Turkey
[c] UNAM-National Nanotechnology Research Center, Bilkent University, 06800 Ankara, Turkey

ARTICLE INFO

Keywords:
Fiber optic pressure sensor
Fabry-Perot interferometry
Acceptance radius
Fungus-shaped center embossed diaphragm

ABSTRACT

A novel structure with a fungus-shaped center embossed diaphragm (FCED) geometry has been proposed to modify in diaphragm-based Fabry-Perot fiber optic pressure sensors (FP-FOPS). The proposed FCED geometry was obtained by adding a pillar between the mesa and diaphragm. Before the simulation analysis of FCED, we derived mathematical equations of attenuation factor widening the acceptance radius. The attenuation factor is defined to understand sensor loss, which is neglected in the literature. With this derived formula, the light reflected from the deflected diaphragm and the light unguided in the fiber was detected. Since the deformation angle is zeroized in the FCED structures, the sensor loss due to the attenuation factor is eliminated. All the incident light being re-guided in the fiber. With FCED design's help, the decreasing sensitivity in the center embossed diaphragms (CED) has been prevented. Moreover, the deviation of the frequency response of FCED remains lower than 1% compared with the results of conventional diaphragms. As a result, it produces a more stable sensor, and the FCED structure is less affected by manufacturing errors. The researchers can benefit from the use of our presented results when designing and producing new diaphragm-based FP-FOPS.

1. Introduction

Fiber optic sensors attract more interest of researchers due to their advantages such as optical isolation, which are EMI/FRI immunity, noise, crosstalk, and ground loop immunity, elimination of spark-shock hazards, useful in explosive environments, low signal attenuation for remote measurements; physical factors which are small in size and mass, resistant to harsh environments, high-temperature tolerance, chemically inert, high tolerance to vibration and shock; and performance characteristics which are high resolution, high dynamic range, excellent linearity, temperature compensation or low-temperature sensitivity, multiplexing capability [1,2]. Thanks to these unique features of fiber optic sensors, they have the considerable potential to be used in many fields such as military, health, environment, construction, etc. [3–7].

Among fiber optic pressure sensors, the most preferred one is the diaphragm-based extrinsic Fabry-Perot (FP) interferometer, which led to smart design depending on the parameters to be measured. It is based on the principle of measuring the phase difference resulting from the reflection of light between two parallel planes due to the oscillation of the diaphragm used as the sensing medium. For this reason, the mechanical properties and geometry of the diaphragm, which affect the sensor's performance, are significant for researchers designing the sensor. The researchers focused on developing new Fabry-Perot fiber optic pressure sensors (FP-FOPSs) trace in two ways; the first is the use of new materials, as a diaphragm [8–11]; the second is to make creative changes to the conventional geometric design of the diaphragm [12–15]. In conventional diaphragm-based FP-FOPS, the diaphragm's center deviates from parallelism when deflection becomes larger. To overcome this problem, researchers try to apply innovative geometries to the diaphragm.

The primary purpose of making changes in the diaphragm's geometry is to produce a more stable FP interferometer with maximum efficiency. In this view, the researchers modified conventional (or circular) diaphragms (CD) with more complex ones. In early studies, a group of researchers was used center embossed (also known as mesa-structured) diaphragms (CED) in FP-FOPS [7,14,16–18]. Fu et al. published an article that the beam-supported membrane structure [13]. Tian et al. designed and produced a square beam-membrane structure in FP-FOPS [16]. Moreover, another diaphragm type is the corrugated structure, which has some difficulties in mass production [12,19]. All these designs

* Corresponding author.
E-mail addresses: sehayber@ahievran.edu.tr (Ş.E. Hayber), umutaydemir@uludag.edu.tr (U. Aydemir).

https://doi.org/10.1016/j.yofte.2020.102429
Received 22 June 2020; Received in revised form 3 November 2020; Accepted 1 December 2020
Available online 19 December 2020

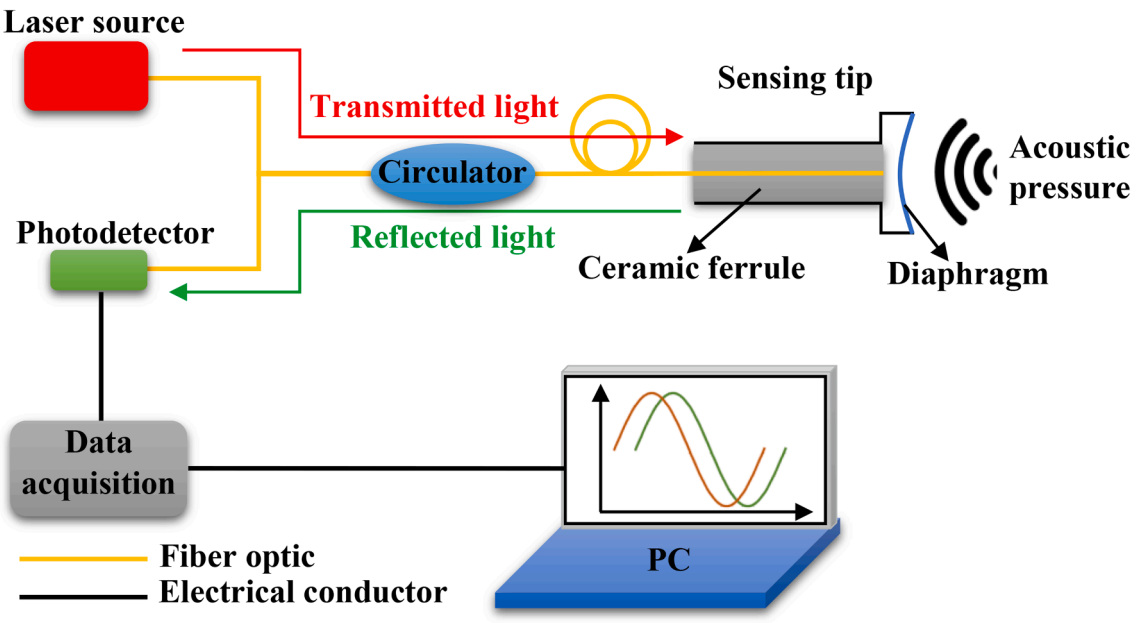

Fig. 1. The sensing mechanism of diaphragm-based FP-FOPS.

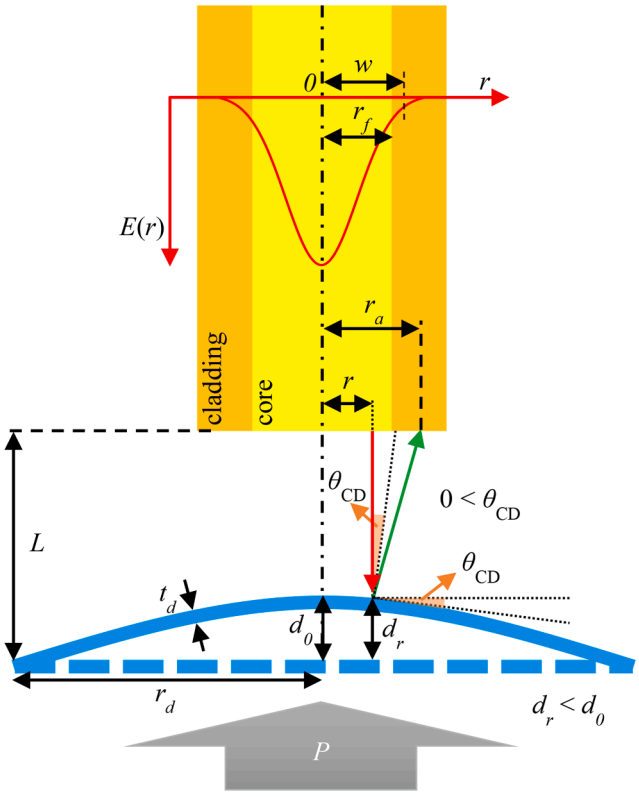

Fig. 2. Schematic representation of the deformation angle formed in the CD after the applied pressure.

bring advantages and disadvantages to the sensor. The diaphragm's complex geometry reveals different parameters, making it challenging to solve the diaphragm's deflection precisely. The researchers also present a mathematical approximation that works under certain conditions to calculate diaphragm deflection [7,14,17].

In the present study, a novel fungus-shaped center embossed diaphragm (FCED) geometry is proposed to zeroize the attenuation factor (*AF*). A mathematical model is developed to calculate the acceptance radius. The proposed FCED geometry obtained by adding a pillar to the CEDs is analyzed with ANSYS simulation software. According to simulations results, the reduced sensitivity in CED has been improved closer to the CD level. Moreover, thanks to the use of FCED, sensor sensitivity is almost independent of the mesa thickness. In addition to the sensitivity results, the frequency response of FCED is understood by examining

modal analysis with ANSYS. It brings FCED the ability to produce more stable sensor sensitivity, and they are less affected by manufacturing errors such as sensor response reductions due to axis shifts during production. The results of the study could be used by researchers when designing and producing diaphragm-based FP-FOPS.

2. Materials and methods

2.1. Presentation of the problem

The schematic diagram of the sensing mechanism of the diaphragm-based FP-FOPS is given in Fig. 1. As shown in Fig. 1, the sensing tip is connected to a laser source and a photodetector via a 2 × 1 single-mode fiber (SMF) optic coupler or circulator. The diaphragm deflects under pressure, and it results in an interference between reflected light and incidence light.

The detailed representation of the sensing tip is given in Fig. 2, consisting of the end of SMF and the reflective diaphragm to sense acoustic pressure in the medium. The deformation angle (θ_{CD}) increases as the diaphragm pressure increases, as seen in Fig. 2. This situation causes the light to scatter to a different point by moving away from the fiber core center. This angle alone is not sufficient to predict the losses that may occur in the interferometer. A basis is formed for the mathematical model by applying geometric optics to the diaphragm seen in Fig. 2.

The d_r is the deflection in any radius on the diaphragm surface, d_0 is the total deflection in the center of the diaphragm, and they can be calculated using Eq. (1) and Eq. (2), respectively [15].

$$d_r = \frac{3(1-v^2)P}{16Et_d^3}\left(r_d^2 - r^2\right)^2 \tag{1}$$

$$d_0 = \frac{3(1-v^2)P}{16Et_d^3}r_d^4, r = 0 \tag{2}$$

Here P is the pressure, r_d is the radius, t_d is the thickness, E is the Young modulus, and v is the Poisson's ratio of the diaphragm. The r is the radial distance from the center of the fiber core. When we view the SMF's end face from the diaphragm surface under pressure, the angle of θ_{CD} occurs between the surface normal of the diaphragm and the SMF normal (see Fig. 2). Fu et al. described this angle in their previous study [13]. As seen in Eq. (3), we have modified this angle with the Fabry-Perot cavity; L. Wang et al. [7] also discussed this angle regarding the mode field radius (w), and we generalized it as Eq. (4).

$$\theta_{CD} = \frac{1}{2}\arctan\left(\frac{r_a - r}{L - d_r}\right) \tag{3}$$

$$\theta_{CD} = \arctan\left(\frac{d_0 - d_r}{r}\right) \tag{4}$$

With the help of Eq. (5), which is a trigonometric identity, Eq. (3) and Eq. (4) are combined, and Eq. (8) is obtained when it is solved for r_a.

$$\frac{1}{2}\arctan(x) = \arctan\left(\frac{x}{1+\sqrt{1+x^2}}\right) \tag{5}$$

$$\theta_{CD} = \frac{1}{2}\arctan\left(\frac{r_a - r}{L - d_r}\right) = \arctan\left(\frac{\frac{r_a - r}{L - d_r}}{1+\sqrt{1+\left(\frac{r_a - r}{L - d_r}\right)^2}}\right) \tag{6}$$

$$\frac{\frac{r_a - r}{L - d_r}}{1+\sqrt{1+\left(\frac{r_a - r}{L - d_r}\right)^2}} = \frac{d_0 - d_r}{r} \tag{7}$$

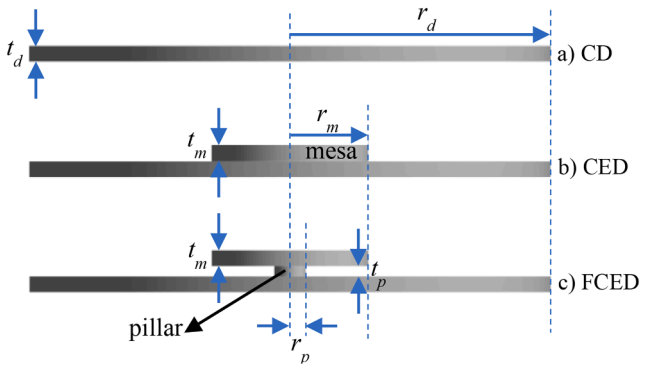

Fig. 3. Diaphragm types of FP-FOPS **(a)** CD, **(b)** CED, and **(c)** FCED.

Table 1
Definition of variables.

Variables	Definition
r	Radius
r_d	Radius of the conventional diaphragm
r_f	Radius of the fiber core
w	Mode field radius of the fiber
$E(r)$	Electric field
r_p	Radius of the pillar
r_m	Radius of the mesa
r_a	Acceptance radius
d_0	Central deflection of the diaphragm
d_r	Deflection at r
L	Fabry-Perot cavity length
t_d	Thickness of the conventional diaphragm
t_p	Thickness of the pillar
t_m	Thickness of the mesa
P	Pressure
θ_{CD}	Deformation angle of the conventional diaphragm
θ_{CED}	Deformation angle of the center embossed diaphragm
θ_{FCED}	Deformation angle of the fungus-shaped center embossed diaphragm
E	Young's modulus of the diaphragm material
v	Poisson ratio of the diaphragm material
ρ	Mass density of the diaphragm material
λ	Wavelength
n	Refractive index of Fabry-Perot medium
ϕ	Phase difference of interferometer

$$r_a = \frac{-d_r^2 r + 2d_r Lr - 2Ld_0 r + d_0^2 r - r^3}{d_r^2 - 2d_r d_0 + d_0^2 - r^2} \tag{8}$$

By simplifying Eq. (8), we figured out Eq. (10), which expresses the acceptance radius (r_a) of FP-FOPSs.

$$r_a = r - \frac{2r(d_r^2 - Ld_r + Ld_0 - d_r d_0)}{(d_0 - d_r)^2 - r^2} \tag{9}$$

$$r_a = r + \frac{2r(L - d_r)(d_0 - d_r)}{r^2 - (d_0 - d_r)^2} \tag{10}$$

$$AF = \frac{2r(L - d_r)(d_0 - d_r)}{r^2 - (d_0 - d_r)^2} > 0 \tag{11}$$

The Eq. (11) causes attenuation of sensor output in r_a is more magnificent than mode field radius (w). When designing FP-FOPS, r_a can be calculated and compared with the value of w of fiber. There is no mathematical model to calculate attenuation factor (AF) and acceptance radius (r_a) of diaphragm-based FP-FOPS. Besides, a recent study addressing sensor losses due to parallelism distortions from a different perspective has been published by Ghildiyal et al. [20].

For step-index single-mode fibers, the mode field radius (w) may be estimated from the core radius r_f and the V number, using Marcuse's equation [21].

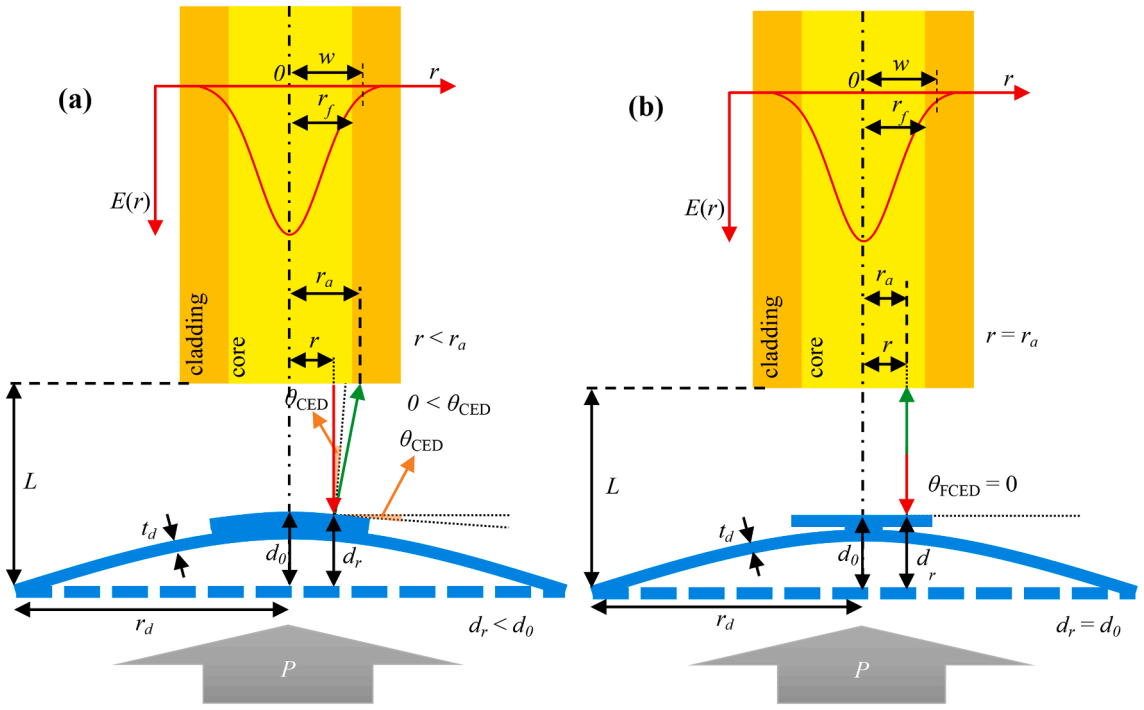

Fig. 4. Schematic representation of deflected **(a)** CED and **(b)** FCED after the applied pressure.

$$\frac{w}{r_f} \approx 0.65 + \frac{1.619}{V^{3/2}} + \frac{2.879}{V^6} \tag{12}$$

V is the normalized frequency of the fiber defined by Eq. (13) [22].

$$V = \frac{2\pi r_f}{\lambda}\sqrt{\left(n_f^2 - n_c^2\right)} \tag{13}$$

The n_f and n_c represent the refractive index of the fiber core and cladding, respectively.

2.2. The design of fungus-shaped center embossed diaphragm (FCED)

The diaphragm types used in this work is seen in Fig. 3. The main reason for *AF* greater than zero in FP-FOPS is the deformation angle formed on the diaphragm's surface. FCED structure is designed as in Fig. 3 (c) to zero this angle. CED was derived by adding mesa to CD, and FCED was derived by adding a pillar to CED. Thanks to the use of pillars, the contact with the main diaphragm are minimized compared to CED structures. These FCED structures have been used in different areas inspired by nature in the literature [23–26]. FP-FOPS parameters and definitions produced with CD, CED, and FCED are given in Table 1.

2.2.1. The deformation angle

In some studies, the researchers claim that flatness of the diaphragm center is essential. They demonstrate that the CED could keep the diaphragm center flat [7,14,16,17]. However, since complete flatness cannot be achieved in CEDs, the deformation angle occurs. The deformation angle of the CED (θ_{CED}) and FCED (θ_{FCED}) under static pressure was given in Fig. 4(a) and (b), respectively. The *AF* in FP-FOPS is desired to be equal to zero. The θ_{FCED} and thus, *AF* parameters are equalized to zero by providing full flatness by using the FCED structure in FP-FOPS. The relation of the deformation angles of diaphragm types is given as $\theta_{CD} > \theta_{CED} > \theta_{FCED} = 0$.

While the FCED structure deflects, its mesa remains flat. Thus, the deformation angles are equal to zero, ensuring that the fiber tip and the diaphragm-formed medium transform into the ideal FP interferometer. As seen in Fig. 4 (b), it can be shown that all the incident light can be reflected from the FCED diaphragm and re-guided in the fiber. In this way, the losses in the amplitude of the optical signal at the detector output are minimized.

2.2.2. The sensitivity

Contrary to the CED, FCED contributes positively to the sensor sensitivity since the contact with the main diaphragm is minimized. The FP cavity length, L variation versus the pressure applied to the diaphragm, is equal to the deflection, d_r in the diaphragm. We can express the mechanical sensitivity as follows [12],

$$S_m = \frac{dL}{dP} = \frac{dd_r}{dP} = \frac{3(1-\nu^2)}{16Et_d^3}\left(r_d^2 - r^2\right)^2 \tag{14}$$

The optical phase difference between the two reflected light in the interferometer is expressed [27].

$$\phi = \frac{4\pi nL}{\lambda} \tag{15}$$

The FP-FOPS's phase sensitivity can be obtained by [28]

$$S_\phi = \frac{d\phi}{dP} = \frac{4\pi n}{\lambda}\frac{dL}{dP} = \frac{4\pi n}{\lambda}S_m = \frac{3\pi n(1-\nu^2)}{4Et_d^3\lambda}\left(r_d^2 - r^2\right)^2 \tag{16}$$

The radius dependent deflection (d_r) of the circular diaphragm was used to express S_m in Eq. (14). Since there is no equation to calculate the deflection value at any r point derived for CEDs, the phase and mechanical sensitivity cannot be calculated based on the radius for CEDs. It is only possible to calculate center deflection and sensitivity for CEDs. As the FCED structure deflection is very close to CD, as seen in the analysis, the Eq. (16) can also be used for FCEDs.

3. Results and discussion

3.1. The acceptance radius induced loss

To calculate the losses in FP-FOPSs made with CD, r_a versus r and L with different pressure were obtained from MATLAB by using Eq. (10) and plotted as Fig. 5. Here r is the radial distance where the light emerges, and L is the FP cavity length. The value of w is obtained as

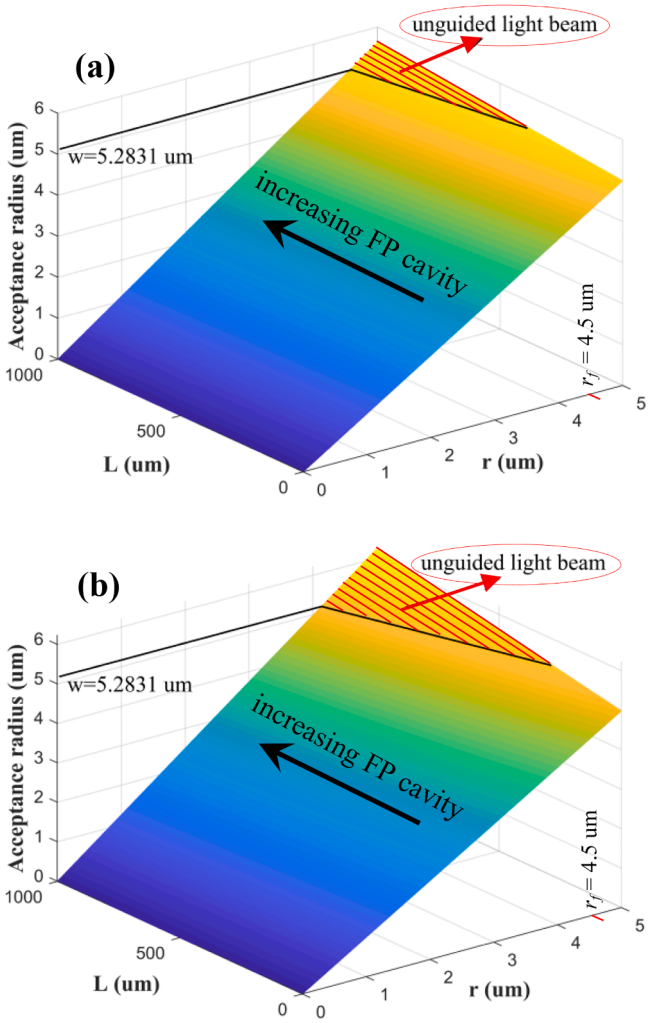

Fig. 5. The acceptance radius versus radius and FP cavity length for CD under the pressure of **(a)** 50 kPa, and **(b)** 100 kPa.

5.2831 μm for $\lambda = 1550$ nm by using Eq. (12) and Eq. (13) for SMF-28e fiber with the value of $n_f = 1.449$, $n_c = 1.444$, $r_f = 4.5$ μm. When calculating r_a for CD made of silica material ($E = 73$ GPa, $\nu = 0.17$, and $\rho = 2200$ kg/m^3) with a relatively thick and not large ($r_d = 500$ μm, $t_d = 10$ μm), the regions where the light cannot be guided at 50 kPa, and 100 kPa pressure values are shown. The unguided light beams, which means loss, are clearly shown in the shaded region for Fig. 5. This loss increases due to the increased FP cavity length, while diaphragm geometry and the material do not change. The amount of loss will further increase at the thin/large diaphragm or high pressures. As a result, as seen in Fig. 5 (a) and (b), it appears that even lights emitted in smaller radii than the fiber core cannot be re-guided for long FP cavities. When looking at Fig. 5(b), the light beams emerged from 4.5 μm cause loss at FP cavity lengths greater than 500 μm. This situation in fiber optic FP interferometers is the deviation of the diaphragm from ideal flatness and parallelism. The results of the study published by Ghildiyal et al. contribute to our results [20]. Although this loss is somewhat reduced in CED, it still appears as a problem that cannot be calculated in the literature. Since the deformation angle on the diaphragm's surface under load cannot be zero, long FP cavity lengths are not allowed. In the FCED structures, $\theta_{FCED} = 0$, all the incident light is re-guided in the fiber, and the loss due to r_a is eliminated.

3.2. The proof of FCED design

To observe the effect of FCED on sensitivity, silica is used in whole diaphragms with values of $E = 73$ GPa, $\nu = 0.17$, and $\rho = 2200$ kg/m^3. In the study, after the analysis of CD ($r_d = 500$ μm and $t_d = 30$ μm), mesa ($r_m = 150$ μm and $t_m = 50$ μm) was added on the same CD and the CED structure was analyzed under the same conditions. Finally, FCED (mesa; $r_m = 150$ μm, $t_m = 30$ μm and pillar; $r_p = 30$ μm and $t_p = 20$ μm) was analyzed.

ANSYS static structural analyzes of these designs, CD, CED, and FCED made by silica, are given in Fig. 6, (a), (b), and (c), respectively. The simulation results showed that the CED structure negatively affects deflection, while this negative effect disappeared in FCED. Also, the flatness required by CED designers has been achieved 100 percent thanks to FCED. This situation is seen from the sensitivity versus r given in Fig. 7. As seen in the figure, while the decrease of sensitivity reaches 50% for CED, the FCED remains closer to the sensitivity of CD.

The performance of diaphragms used in the literature is compared with CD or flat diaphragm (FD). As shown in Fig. 8, the sensitivity comparison of all diaphragm types used in the literature and the recommended structure of FCED is given. The sensitivity value of beam supported diaphragm (BSD) and corrugated diaphragm (COD), which are difficult to manufacture and used in a few studies, is higher than CD/FD [12,13,15,16,19]. However, the sensitivity of the more commonly used CEDs is less than CD/FD, as can be seen from figure [7,14,17]. The

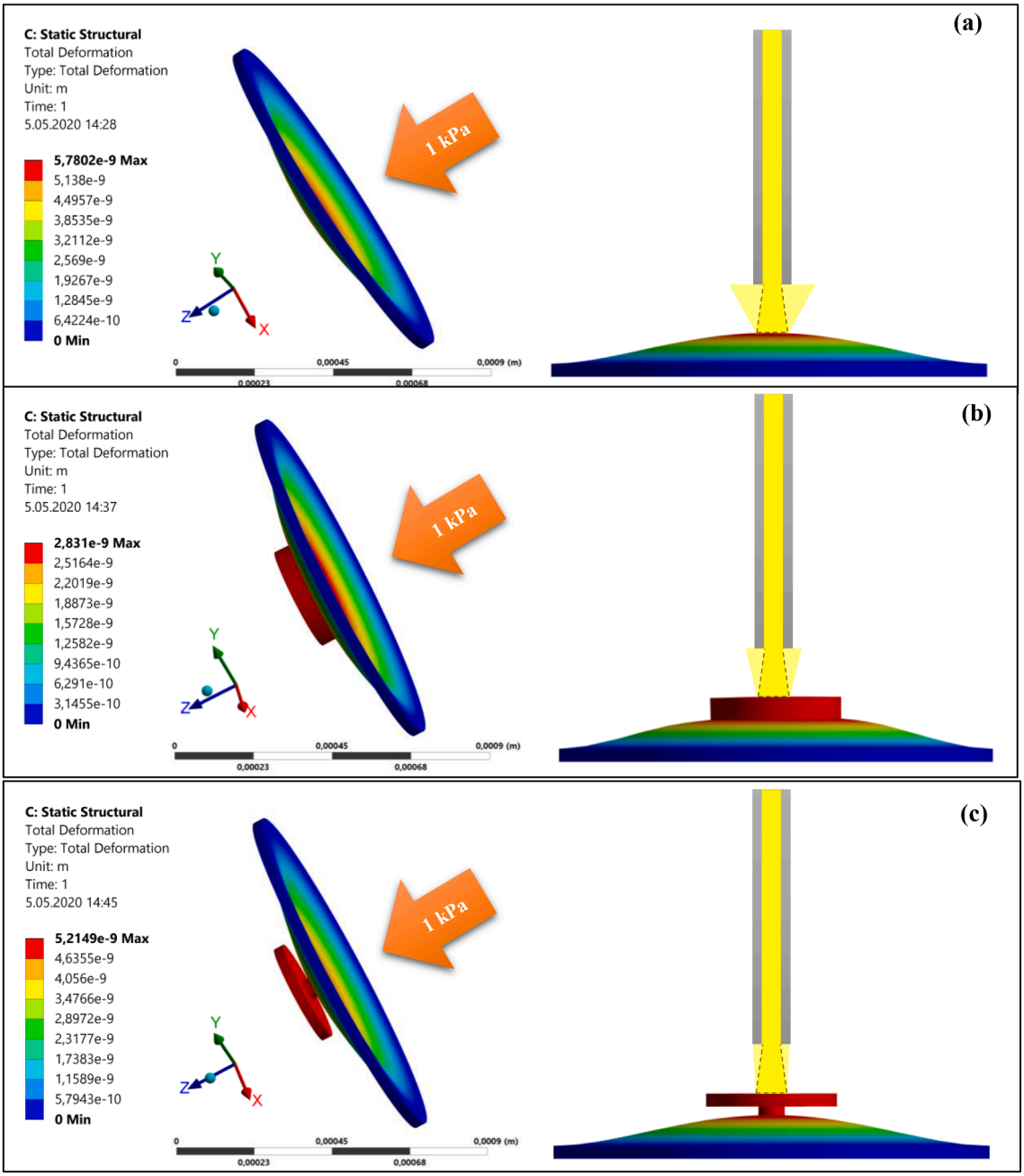

Fig. 6. ANSYS static structural analysis of diaphragm deflection for **(a)** CD, **(b)** CED, and **(c)** FCED.

sensitivity of FCED suggested in the study is approximate to CD/FD.

3.3. The effect of FCED on sensor parameters

When using the same material for all diaphragm types, only the effect of diaphragm geometry on sensor sensitivity was analyzed in the previous section. The material properties and geometric dimensions of the diaphragms analyzed in ANSYS simulations are given as in Table 2, considering the MEMS production processes. With the use of FCED, four geometric variables to be analyzed are revealed, excluding the radius and thickness of the main diaphragm. Since the difference between FCED and CED is a pillar, the effect of the pillar was examined first. It is observed that the effect of t_p is negligible for different values. This result published by Sun et al. is consistent with the effect of mesa thickness in CED [14]. Sensitivity and frequency versus pillar radius plots of FCED in different mesa dimensions were analyzed with static structure and modal analysis. While the radius of the pillar increase in the specified radius and the thickness of the mesa, the value of sensitivity and frequency were given in Fig. 9(a)-(c) and (d)-(f), respectively. As the mesa radius increases, the sensitivity, which we emphasize as an advantage in FCEDs, decreases. Contrary to sensitivity, as the mesa radius increases, the fundamental resonance frequency slightly increases. For this reason, a low mesa radius should be preferred in FCED structures. When the analysis is compared by adding mesa having different sizes on the pillar, it is seen that although the radius of the pillar increase, there is no significant change in sensor sensitivity and frequency response. The change of the diaphragm geometry does not lead to changes in the sensor parameter, which emerges as a positive contribution with the FCED structure. In practice, the CED structures were intentionally or unintentionally occurred by researchers to increase the diaphragm reflectivity, maintain flatness, or use different purposes. Thus, re-calibration or re-design caused by the change in the sensing parameters of the

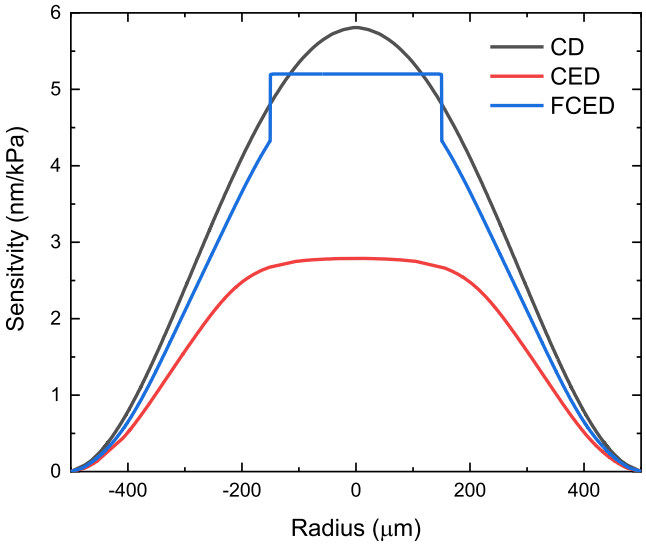

Fig. 7. The sensitivity versus radius plots of CD, CED, and FCED.

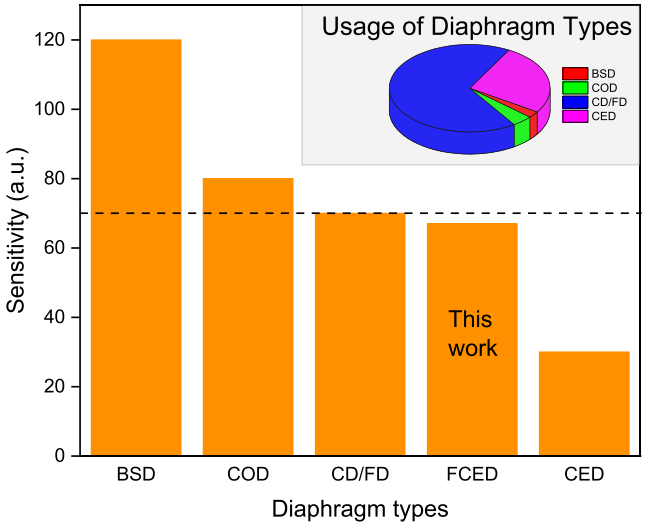

Fig. 8. Sensitivity plot of diaphragm types for FP-FOPSs *(dashed line is the reference value of CD/FD)*. Inset: Usage of diaphragm types for FP-FOPSs in the literature.

sensor is eliminated by using FCED in FP-FOPS.

The effect of pillar radius on sensitivity and frequency in certain mesa radius has been discussed in the previous paragraph. Since sensitivity loss is an undesirable situation, $r_m = 50$ μm was chosen for future analyzes. The proposed FCED structure was compared with the CD and CED structures; we focused on the mesa thickness in detail. In the literature, it is a fact that mesa reduces the sensitivity and changes the resonance frequency of CEDs. The deflection for FCED structures with the same mesa dimensions of the CED structure is seen in Fig. 10(a) (*deflection of CD was marked as a red dashed line in the figure*). The undesirable decrease of sensitivity in CED structures has been prevented thanks to the FCED design. To express and compare the deviation of sensitivity from the conventional diaphragm in percent, Fig. 10(b) was given. It can be seen from the figure that the deviation of CED structures varies between 9 and 20 %, while this deviation in FCED structures remains around 2–5%. In recently published studies, beam supported

Table 2
The parameters used in the simulation.

	CD	CED		FCED		
	diaphragm	**diaphragm**	**mesa**	**diaphragm**	**pillar**	**mesa**
material	Si	Si	SiO_2	Si	SiO_2	Si
E	170 GPa	170 GPa	73 GPa	170 GPa	73 GPa	170 GPa
V	0.3	0.3	0.17	0.3	0.17	0.3
ρ	2350 kg/m^3	2350 kg/m^3	2200 kg/m^3	2350 kg/m^3	2200 kg/m^3	2350 kg/m^3
radius	500 μm	500 μm	50–150 μm	500 μm	10–120 μm	50–150 μm
thickness	30 μm	30 μm	5–30 μm	30 μm	1–5 μm	5–30 μm

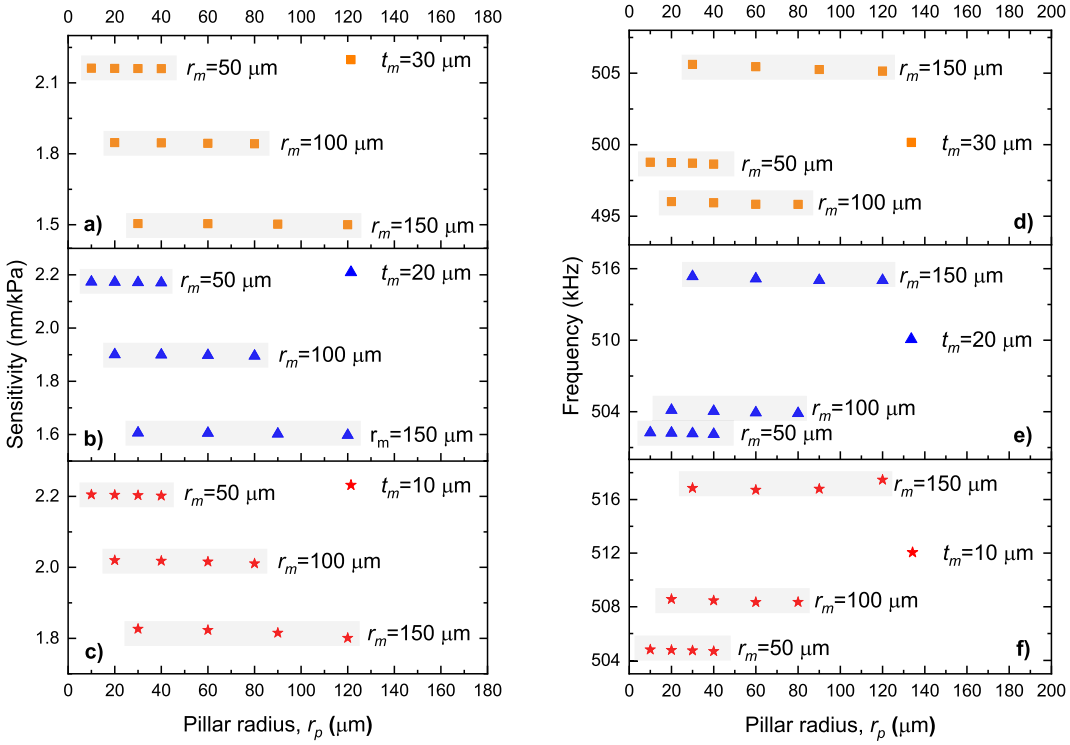

Fig. 9. The sensitivity and frequency versus pillar radius plots of FCED for $t_p = 1$ μm.

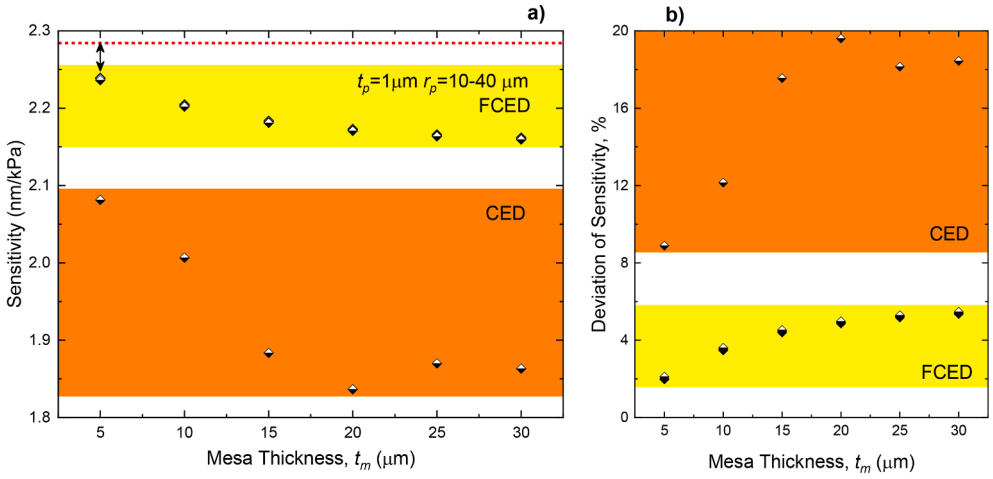

Fig. 10. **(a)** The sensitivity versus mesa thickness plots of CED, and FCED, **(b)** Deviation of sensitivity versus mesa thickness plots of CED and FCED. (*reference line is given for CD;* $r_m = 50$ μm *for CED and FCED*).

membrane, and corrugated structures have higher sensitivity than the CD [12,13,15,16,19,28]. However, the MEMS production processes of these structures are more complex and difficult [12]. Thus, their usage is limited among other diaphragm types, as seen in the inset of Fig. 8.

To compare the proposed FCED structure's frequency response, modal analysis was carried out, and results were plotted in Fig. 11(a) (*frequency response of CD was marked as red dashed line in the figure*). Interestingly, the frequency response of the FCED structure independently from mesa dimensions and the frequency response of the CD structure overlapped each other. Fig. 11(b) shows the percentage deviation in CED structure and FCED structure's frequency response. Employing the FCED structure, the deviation in frequency response remains at a maximum of 1%, while this deviation is around 4–9% for CED structures. Since this causes a re-design in the sensors to be designed for narrowband applications, the FCED structure will not require this re-design. In our analysis, the mesa's radius in CED and FCED structures was selected as sufficiently large (50 μm), corresponding to 10% of the diaphragm radius. The frequency response of FCED was demonstrated and compared with the value of CED's.

4. Conclusion

In the present study, a novel FCED structure was demonstrated for FP-FOPS. The disadvantages caused by the integrity of the mesa and the diaphragm in the CED have been prevented. In practice, the CED structures intentionally or unintentionally occur in experiments. The mesa structure used to improve optical sensitivity in CEDs is produced in full contact with the main diaphragm, which determines the sensor's mechanical properties. In this study, the mesa used to minimize optical losses was separated from the FCED structure's diaphragm. Thus, while

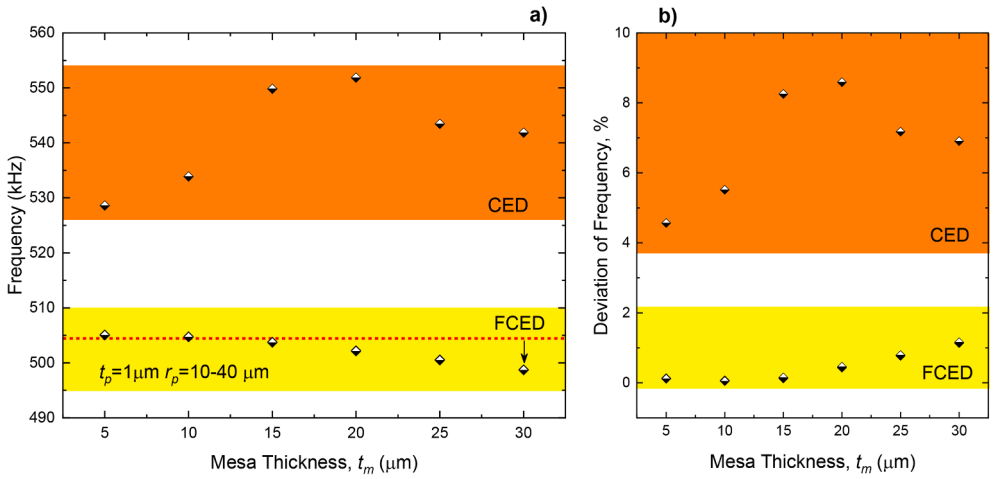

Fig. 11. **(a)** The frequency versus mesa thickness plots of CED, and FCED, **(b)** Deviation of frequency versus mesa thickness plots of CED and FCED. (*reference line is given for CD;* $r_m = 50$ *μm for CED and FCED*).

the mesa fulfills its duty fully, the mesa's negative impact on the main diaphragm was eliminated. By means of FCED structure, 100% flatness was achieved, and the deflection and resonance frequency were approximated to the CD's values. The perfect discrete structure, FCED, was created by adding a pillar between the mesa and the main diaphragm. The advantages of using FCED is concluded as below list.

- The mathematical model was derived from understanding the deformation angle in FP-FOPS.
- The attenuation factor and acceptance radius are defined depending on all parameters of FP-FOPS.
- The deformation angle was zeroized using the FCED structure in FP-FOPS.
- By using the FCED, the mesa and main diaphragm were separated to eliminate negative effects such as optic loss, decrease in sensitivity, frequency shifting on each other.
- FCED structure allows large FP cavity length.
- The disadvantages of production induced eccentric structures were minimized.
- The deflection and frequency response became independent by the mesa sizes in FCED structures.

When the Fabry-Perot cavity is medium rather than air, water, the acceptance angle of the fiber decreases, and FCED becomes more critical. Similarly, as the wavelength of the light used in the sensor decreases, the typical value of 1310 nm instead of 1550 nm decreases the mode field radius. The micro-fabrication of the proposed FCED structures and its advantages above concluded on sensor performance will be experimentally demonstrated in the future study.

Declaration of Competing Interest

The authors declare that they have no known competing financial interests or personal relationships that could have appeared to influence the work reported in this paper.

Acknowledgments

This work was supported by the Scientific Research Fund of the Uludağ University under the project number BUAP (MH)-2019/1. The authors would like to thank FOSENS Electro Optic Technologies to support the staff's research activities.

References

[1] H.M. Hashemian, C.L. Black, J.P. Farmer, Assessment of fiber optic pressure sensors (No. NUREG/CR-6312). Nuclear Regulatory Commission, Washington, DC (United States). Div. of Systems Technology; Analysis and Measurement Services Corp., Knoxville, TN (United States) (1995).
[2] E. Udd, W.B. Spillman Jr., Fiber optic sensors: an introduction for engineers and scientists, John Wiley & Sons, 2011.
[3] M.d. Islam, M. Ali, M.-H. Lai, K.-S. Lim, H. Ahmad, Chronology of Fabry-Perot Interferometer Fiber-Optic Sensors and Their Applications: A Review Sensors 14 (4) (2014) 7451–7488, doi: 10.3390/s140407451.
[4] S. Ghildiyal, R. Balasubramaniam, J. John, Diamond turned micro machined metal diaphragm based Fabry Perot pressure sensor, Opt. Laser Technol. 128 (2020) 106243, https://doi.org/10.1016/j.optlastec.2020.106243.
[5] S.E. Hayber, S. Keser, 3D sound source localization with fiber optic sensor array based on genetic algorithm, Opt. Fiber Technol. 57 (2020) 102229, https://doi.org/10.1016/j.yofte.2020.102229.
[6] P. Roriz, O. Frazão, A.B. Lobo-Ribeiro, J.L. Santos, J.A. Simões, Review of fiber-optic pressure sensors for biomedical and biomechanical applications, J. Biomed. Opt 18 (5) (2013) 050903, https://doi.org/10.1117/1.JBO.18.5.050903.
[7] F. Wang, Z. Shao, J. Xie, Z. Hu, H. Luo, Y. Hu, Extrinsic Fabry-Pérot underwater acoustic sensor based on micromachined center-embossed diaphragm, J. Lightwave Technol. 32 (23) (2014) 4628–4636.
[8] S.E. Hayber, U. Aydemir, T.E. Tabaru, O.G. Saracoglu, The Experimental Validation of Designed Fiber Optic Pressure Sensors With EPDM Diaphragm, IEEE Sensors J. 19 (14) (2019) 5680–5685, https://doi.org/10.1109/JSEN.2019.2908410.
[9] S.E. Hayber, T.E. Tabaru, U. Aydemir, O.G. Saracoglu, Use of 2D In 2 Se 3 Single Crystal as a Diaphragm Material for Fabry-Perot Fiber Optic Acoustic Sensors, J. Nanoelectron. Optoelectron. 14 (4) (2019) 464–469, https://doi.org/10.1166/jno.2019.2544.
[10] Q. Cui, P. Thakur, C. Rablau, I. Avrutsky, M.-C. Cheng, Miniature Optical Fiber Pressure Sensor With Exfoliated Graphene Diaphragm, IEEE Sensors J. 19 (14) (2019) 5621–5631, https://doi.org/10.1109/JSEN.2019.2904020.
[11] F. Yu, Q. Liu, X. Gan, M. Hu, T. Zhang, C. Li, F. Kang, M. Terrones, R. Lv, Ultrasensitive Pressure Detection of Few-Layer MoS 2, Adv. Mater. 29 (4) (2017) 1603266, https://doi.org/10.1002/adma.201603266.
[12] H. Li H. Deng G. Zheng M. Shan Z. Zhong B. Liu Reviews on Corrugated Diaphragms in Miniature Fiber-Optic Pressure Sensors Applied Sciences 9 11 2241 10.3390/app9112241.
[13] C. Fu, W. Si, H. Li, D. Li, P. Yuan, Y. Yu, A Novel High-Performance Beam-Supported Membrane Structure with Enhanced Design Flexibility for Partial Discharge Detection Sensors 17 (3) (2017) 593, doi: 10.3390/s17030593.
[14] Y. Sun, G. Feng, G. Georgiou, E. Niver, K. Noe, K. Chin, Center embossed diaphragm design guidelines and Fabry–Perot diaphragm fiber optic sensor, Microelectron. J. 39 (5) (2008) 711–716, https://doi.org/10.1016/j.mejo.2007.12.020.
[15] S.E. Hayber, T.E. Tabaru, O.G. Saracoglu, A novel approach based on simulation of tunable MEMS diaphragm for extrinsic Fabry–Perot sensors, Opt. Commun. 430 (2019) 14–23, https://doi.org/10.1016/j.optcom.2018.08.021.
[16] B. Tian, F. Zhan, F. Han, K. Li, N.a. Zhao, N. Yang, Z. Jiang, An optical fiber Fabry–Pérot micro-pressure sensor based on beam-membrane structure, Meas. Sci. Technol. 29 (12) (2018) 125104, https://doi.org/10.1088/1361-6501/aadfb1.
[17] Y. Ge, M. Wang, H. Yan, Optical MEMS pressure sensor based on a mesa-diaphragm structure, Opt. Express 16 (26) (2008) 21746, https://doi.org/10.1364/OE.16.021746.
[18] Y. Ge, T. Wang, J. Zhang, J. Chang, Wavelength-demodulation MEMS Fabry Perot temperature sensor based on bimetallic diaphragm, Optik 127 (12) (2016) 5040–5043, https://doi.org/10.1016/j.ijleo.2016.02.050.

[19] J. Zhu, M. Wang, L.u. Chen, X. Ni, H. Ni, An optical fiber Fabry–Perot pressure sensor using corrugated diaphragm and angle polished fiber, Opt. Fiber Technol. 34 (2017) 42–46, https://doi.org/10.1016/j.yofte.2016.12.004.
[20] S. Ghildiyal, R. Balasubramaniam, J. John, Effect of flatness and parallelism errors on fiber optic Fabry Perot Interferometer of low to moderate finesse and its experimental validation, Opt. Fiber Technol. 60 (2020) 102372, https://doi.org/10.1016/j.yofte.2020.102372.
[21] D. Marcuse, Loss analysis of single-mode fiber splices. Bell Syst. Tech. J., 56 (5) (1977) 703–718.
[22] D. Marcuse, J. Stone, Coupling efficiency of front surface and multilayer mirrors as fiber-end reflectors, J. Lightwave Technol. 4 (4) (1986) 377–381, https://doi.org/10.1109/JLT.1986.1074729.
[23] P. Amiri, Z. Kordrostami, H. Ghoddus, Design and simulation of a flat cap mushroom shape microelectromechanical systems piezoelectric transducer with the application as hydrophone. IET Sci. Measurement Tech., 14 (2) (2020) 157–164.
[24] M.A. Shah, I.A. Shah, D.-G. Lee, S. Hur, Design Approaches of MEMS Microphones for Enhanced Performance, J. Sensors 2019 (2019) 1–26, https://doi.org/10.1155/2019/9294528.
[25] M.R. Mahlooji, J. Koohsorkhi, Static analysis and simulation of piston coupled diaphragm for microelectromechanical systems based high sensitive sensors. Micro Nano Lett., 13 (6) (2018) 811–816.
[26] H. Gharaei, J. Koohsorkhi, Design and characterization of high sensitive MEMS capacitive microphone with fungous coupled diaphragm structure, Microsyst. Technol. 22 (2) (2016) 401–411, https://doi.org/10.1007/s00542-014-2406-2.
[27] G. Wei, Q.i. Jiang, T. Zhang, A flexible force sensor based on spheroidal Fabry-Perot micro-cavity, Optik 181 (2019) 483–492, https://doi.org/10.1016/j.ijleo.2018.12.101.
[28] B. Liu, H. Zhou, L. Liu, X. Wang, M. Shan, P. Jin, Z. Zhong, An Optical Fiber Fabry-Perot Microphone Based on Corrugated Silver Diaphragm, IEEE Trans. Instrum. Meas. 67 (8) (2018) 1994–2000, https://doi.org/10.1109/TIM.2018.2809840.